

## *Electronic Supplementary Information*

### **Nitrogen-Rich 1T'-MoS<sub>2</sub> Layered Nanostructures Using Alkyl Amines for High Catalytic Performance of Hydrogen Evolution**

*In Hye Kwak,<sup>a</sup> Ik Seon Kwon,<sup>a</sup> Hafiz Ghulam Abbas,<sup>b</sup> Gabin Jung,<sup>a</sup> Yeron Lee,<sup>a</sup> Tekalign Terfa Debela,<sup>c</sup> Seung Jo Yoo,<sup>d</sup> Jin-Gyu Kim,<sup>d</sup> Jeunghye Park,<sup>\*a</sup> and Hong Seok Kang<sup>\*e</sup>*

<sup>a</sup> Department of Chemistry, Korea University, Sejong 339-700, Republic of Korea; E-mail address: [parkjh@korea.ac.kr](mailto:parkjh@korea.ac.kr)

<sup>b</sup> Department of Nanoscience and Nanotechnology, Jeonbuk National University Chonju, Chonbuk 560-756, Republic of Korea.

<sup>c,e</sup> Institute for Application of Advanced Materials, Jeonju University, Chonju, Chonbuk 55069, Republic of Korea.

<sup>d</sup> Division of Electron Microscopic Research, Korea Basic Science Institute, Daejeon 305-806, Republic of Korea.

<sup>e</sup> Department of Nano and Advanced Materials, Jeonju University, Chonju, Chonbuk 55069, Republic of Korea; E-mail address: [hsk@jj.ac.kr](mailto:hsk@jj.ac.kr)

## **Contents**

### **I. Supplementary Tables.**

**Table S1.** Composition of samples determined by elemental analysis.

**Table S2.** Fitted parameters of EXAFS data.

**Table S3.** Fitted parameter of EIS.

**Table S4.** Summary of HER performance of MoS<sub>2</sub> samples synthesized at pH 11.

**Table S5.** Comparison of HER performance with other works.

**Table S6.** Lattice parameters and energies of various configurations of N-doped MoS<sub>2</sub>.

### **II. Supplementary Figures**

**Figure S1.** TEM images of MoS<sub>2</sub> synthesized at pH 3 –13.

**Figure S2.** Raman spectra.

**Figure S3.** TGA and DSC data.

**Figure S4.** XPS survey and valence spectra.

**Figure S5.** XPS of amine HCl salt.

**Figure S6.** NMR data.

**Figure S7.** Chronoamperometric responses of HER.

**Figure S8.** Cyclic voltammograms data.

**Figure S9.** HER performance of MoS<sub>2</sub> synthesized at pH = 11.

**Figure S10.** Structure analysis and HER performance of MoS<sub>2</sub> synthesized at 220 °C.

**Figure S11.** DOS of undoped and N-doped (4×2) MoS<sub>2</sub> supercells.

**Figure S12.** Structures of (4×2) MS-N3T system in configuration A for Volmer reaction.

**Figure S13.** Relative energy of (4×2) MS-N3T system in configuration A versus reaction coordinate for Volmer reaction.

### **III. References**

## I. Supporting Tables

**Table S1.** Composition (mole %) of samples determined by elemental analysis.

Sample <sup>a</sup>	[H]	[C]	[N]	[S]	[N]/[S]	XPS [N]/[S] <sup>a</sup>
MS-0	39.2	3.6	0.63	56.6	0.011	0
MS-N1	39.0	10.8	3.7	46.5	0.079	0.056
MS-N2	46.0	9.8	5.6	38.6	0.15	0.13
MS-N3	44.3	13.2	6.7	36.0	0.19	0.15
MS-N4	45.0	14.7	7.7	32.6	0.24	0.18

<sup>a</sup> [N]/[S] ratio obtained using XPS

**Table S2.** Fitting parameters of EXAFS data for the MoS<sub>2</sub> samples (see Fig. 2).

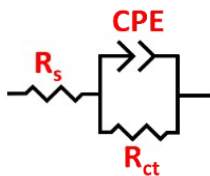
Sample	Scattering Path	$R$ (Å) <sup>a</sup>	CN <sup>b</sup>	$\Delta E$ (eV) <sup>c</sup>	$\sigma^2$ (Å <sup>2</sup> ) <sup>d</sup>
<b>MS-0</b>	Mo-S	2.40	$6.2 \pm 0.3$	2.7	0.0028
	Mo-Mo	3.16	$4.2 \pm 0.1$	2.6	0.0036
<b>MS-N1</b>	Mo-S	2.40	$5.0 \pm 0.3$	-1.4	0.0078
	Mo-Mo	2.76	$1.7 \pm 0.5$	-2.0	0.0091
<b>MS-N2</b>	Mo-S	2.39	$5.2 \pm 0.6$	-5.2	0.0089
	Mo-Mo	2.77	$0.9 \pm 0.4$	2.2	0.0042
<b>MS-N3</b>	Mo-S	2.38	$5.2 \pm 0.6$	-5.8	0.0089
	Mo-Mo	2.78	$0.9 \pm 0.4$	2.7	0.0040
<b>MS-N4</b>	Mo-S	2.38	$4.5 \pm 0.5$	-5.0	0.0078
	Mo-Mo	2.78	$1.0 \pm 0.5$	1.6	0.0053

<sup>a</sup> Distance between scattering atoms.

<sup>b</sup> Coordination number of Mo atoms.

<sup>c</sup> Edge energy shift, representing between the energy grids of experimental and theoretical data.

<sup>d</sup> Debye-Waller factor, which measure the static and thermal disorder, is three-times larger for the intercalated MS samples than MS-0. It suggests that the intercalation produces a broad range of Mo-S and Mo-Mo distances.

**Table S3.** Fitting parameters for Nyquist plot using equivalent circuit shown below.

Sample	$R_s$ ( $\Omega$ )	CPE (mF)	$R_{ct}$ ( $\Omega$ )	$n$	$C_{dl}$ (mF)	$C_{dl}$ (mF cm <sup>-2</sup> )
MS-0	7.5	2.7	913	0.94	2.3	14.0
MS-N1	6.9	3.7	173	0.95	4.7	28.3
MS-N2	6.5	5.1	139	0.96	5.8	35.1
MS-N3	6.2	6.1	60.8	0.98	7.0	43.5
MS-N4	6.1	8.1	40.9	0.96	8.1	49.3

The fitting parameter  $R_s$  represents the internal resistance (electrolyte), CPE is a constant-phase element related to the double-layer capacitance, and  $R_{ct}$  is associated with the charge-transfer resistance from any residual Faradaic processes. The double layer capacitance ( $C_{dl}$ ) can be calculated using the CPE parameter by the equation:  $C_{dl} = (CPE \times R_{ct})^{1/n}/R_{ct}$ , where  $n = 0-1$  (should be  $> 0.75$  for reasonable confidence in  $C_{dl}$ ). The  $n$  values are close to 1. Taken the area of GC RDE electrode ( $=0.1641$  cm<sup>2</sup>), the  $C_{dl}$  value in a unit of mF cm<sup>-2</sup> was obtained, which is about twice of that determined using EIS. Nevertheless, both  $C_{dl}$  values increases consistently with increasing N number.

**Table S4.** HER performance of MoS<sub>2</sub> samples synthesized at pH 11.

Sample No.	pH	$\eta_{J=10}$ <sup>a</sup>	$b$ <sup>b</sup>	$R_{ct}$ ( $\Omega$ ) <sup>c</sup>	$C_{dl}$ (mF cm <sup>-2</sup> ) <sup>d</sup>
MS-N2	11.1	0.22	48	230	13.2
MS-N3	11.2	0.20	45	104	15.0
MS-N4	11.3	0.18	40	83	16.3

<sup>a</sup> Overpotential at  $J=10$  mA cm<sup>-2</sup>, <sup>b</sup> Tafel slope derived from the Tafel equation:  $\eta = b \log(J/J_0)$ , where  $\eta$  is the overpotential (measured),  $b$  is the Tafel slope (mV dec<sup>-1</sup>),  $J$  is the current density (measured), and  $J_0$  is the exchange current density (mA cm<sup>-2</sup>), <sup>c</sup> Charge transfer resistance obtained by fitting the Nyquist plot using the equivalent circuit shown in Fig. 5c, <sup>d</sup> Double-layer capacitance as shown in Fig. S9.

**Table S5.** Comparison of HER performance (in pH 0) of MoS<sub>2</sub> (with no carbon support at pH 0) in the literatures (N/A: Not applicable).

Reference	Materials	Phase	$E_{J=10}$ (mV) at 10 mA cm <sup>-2</sup>	Tafel slope (mV dec <sup>-1</sup> )
S1	Defect-rich MoS <sub>2</sub> nanosheet	2H	190	50
S2	Conducting MoS <sub>2</sub>	1T	200	40
S3	Oxygen-Incorporated MoS <sub>2</sub>	2H	187	55
S4	Edge-terminated MoS <sub>2</sub> nanosheet	2H	149	49
S5	Strained MoS <sub>2</sub> nanosheet	2H	170	60
S6	Ammoniated MoS <sub>2</sub>	1T	320	45
S7	1T MoS <sub>2</sub> single-layer nanosheets	1T	N/A	45
S8	Metallic phase MoS <sub>2</sub> nanosheet	1T	175	41
S9	1T MoS <sub>2</sub> nanosheet	1T	154	43
S10	Ammonia-MoS <sub>2</sub>	N/A	200	55
S11	ALD-MoS <sub>2</sub>	2H	N/A	79
S12	1T' MoS <sub>2</sub> monolayer	1T'	300	83
S13	1T/2H MoS <sub>2</sub>	1T/2H	234	46
S14	Zn- MoS <sub>2</sub>	2H	N/A	51
S15	Functionalized metallic MoS <sub>2</sub> nanosheet	1T	348	75
S16	1T MoS <sub>2</sub> nanodot	1T	173	53
S17	Li-MoS <sub>2</sub>	1T/2H	240	48
Present work	TETA-intercalated MoS <sub>2</sub> (MS-N4)	1T'	170	36

**Table S6.** Parameters of N-doped MoS<sub>2</sub> systems (MS-N1T and MS-N3T) in the 2H or 1T' phases. Concentration of intercalated amine is 12.5%, and concentration of doped N atoms is same as that of sulfur vacancies (C<sub>VS</sub>).

Guest	$N_{VS}^a$ ( $C_{VS}$ )	$P^b$	Size <sup>c</sup>	$C^d$	$a, b, c$ (Å) $\alpha, \beta, \gamma$ (°) <sup>e</sup>	$E_{rel}$ (eV) <sup>f</sup>	$I_{Mo-N}$ (Å) <sup>g</sup>	$I_{Mo-Mo}$ (Å) <sup>g</sup>	$I_{Mo-S}$ (Å) <sup>g</sup>
None	8 (25%)	2H	4×2	R <sub>0</sub>	12.10, 6.20, 12.77 90.0, 90.0, 120.0	0.00	1.99 (1.98, 1.98, 2.00)	2.97 (2.93, 2.93, 2.96, 2.96, 2.96, 3.10)	2.40 (2.37, 2.38, 2.39, 2.40, 2.41, 2.43)
			4×2	A	12.26, 6.15, 12.25 90.0, 90.0, 120.0	1.62	2.00 (2.05, 1.96, 1.98)	3.00 (2.94, 2.95, 2.97, 2.99, 3.03, 3.14)	2.39 (2.36, 2.37, 2.38, 2.40, 2.41, 2.43)
None	8 (25%)	1T'	4×2	R <sub>0</sub>	12.69, 6.51, 12.16 91.4, 95.0, 120.7	9.56	1.95 (1.96, 1.95, 1.95)	2.73 (2.66, 2.68, 2.85, 2.70, 2.75, 2.72)	2.41 (2.33, 2.38, 2.39, 2.40, 2.45, 2.49)
			4×2	R <sub>1</sub>	12.69, 6.51, 12.10 90.0, 90.0, 119.0	11.52	1.97 (1.89, 1.99, 2.14)	2.70 (2.59, 2.60, 2.66, 2.66, 2.94, 2.76)	2.39 (2.34, 2.36, 2.37, 2.41, 2.43, 2.45)
			4×2	A	13.04, 6.36, 12.01 90.0, 90.0, 119.0	10.74	2.00 (1.98, 1.91, 2.11)	2.76 (2.62, 2.67, 2.76, 2.77, 2.85, 2.87)	2.42 (2.39, 2.38, 2.40, 2.41, 2.46, 2.48)
MA	8 (12.5%)	1T'	4×4	A	12.73, 12.95, 17.41, 90.0, 90.0, 119.0	0.00	2.05 (1.85, 2.05, 2.25)	2.91 (2.85, 2.83, 2.91, 2.93, 2.97, 2.99)	2.39 (2.35, 2.37, 2.38, 2.40, 2.41, 2.44)
			4×4	R <sub>0</sub>	12.79, 13.08, 16.50 90.0, 90.0, 119.0	0.72	2.00 (1.94, 2.02, 2.03)	2.76 (2.65, 2.70, 2.72, 2.77, 2.84, 2.90)	2.38 (2.31, 2.34, 2.38, 2.40, 2.41, 2.43)
			4×4	R <sub>1</sub>	12.72, 13.10, 19.00 90.0, 90.0, 119.0	2.27	1.99 (1.86, 2.01, 2.10)	2.86 (2.71, 2.78, 2.79, 2.92, 2.97, 3.01)	2.40 (2.34, 2.37, 2.38, 2.41, 2.43, 2.44)
DETA	8 (25%)	1T'	4×2	A	12.44, 6.44, 19.46 94.9, 75.4, 118.3	0.00	1.99 (1.86, 2.01, 2.10)	2.74 (2.67, 2.78, 2.78, 2.78, 2.86, 2.66)	2.41 (2.31, 2.38, 2.39, 2.43, 2.45, 2.48)
			4×2	R <sub>0</sub>	12.73, 6.54, 18.61 83.8, 98.7, 120.8	0.45	1.89 (1.87, 1.88, 1.93)	2.73 (2.64, 2.66, 2.69, 2.71, 2.83, 2.84)	2.42 (2.30, 2.34, 2.37, 2.38, 2.39, 2.42)
			4×2	R <sub>1</sub>	12.83, 6.53, 19.33 90.0, 90.0, 119.0	0.59	1.89 (1.93, 1.99, 2.03)	2.77 (2.68, 2.69, 2.74, 2.75, 2.86, 2.90)	2.40 (2.35, 2.39, 2.40, 2.41, 2.42, 2.47)

<sup>a</sup>  $N_{VS}$  and  $C_{VS}$  represent the number of S vacancies and their concentration (in parentheses), respectively. <sup>b</sup> Phase (2H or 1T'). <sup>c</sup> Size of the supercell. <sup>d</sup> In configurations R<sub>0</sub> and R<sub>1</sub>,

vacancies form contiguous rows along specific directions in two layers of MoS<sub>2</sub> in the supercell. In configuration A, the vacancies are distributed so that they are four bonds apart from one another. <sup>e</sup> Optimized lattice parameters. <sup>f</sup> Relative energy with respect to the most stable configuration. <sup>g</sup> Nearest distance between two atoms, the average value was obtained from values in the parenthesis.

## II. Supporting Figures

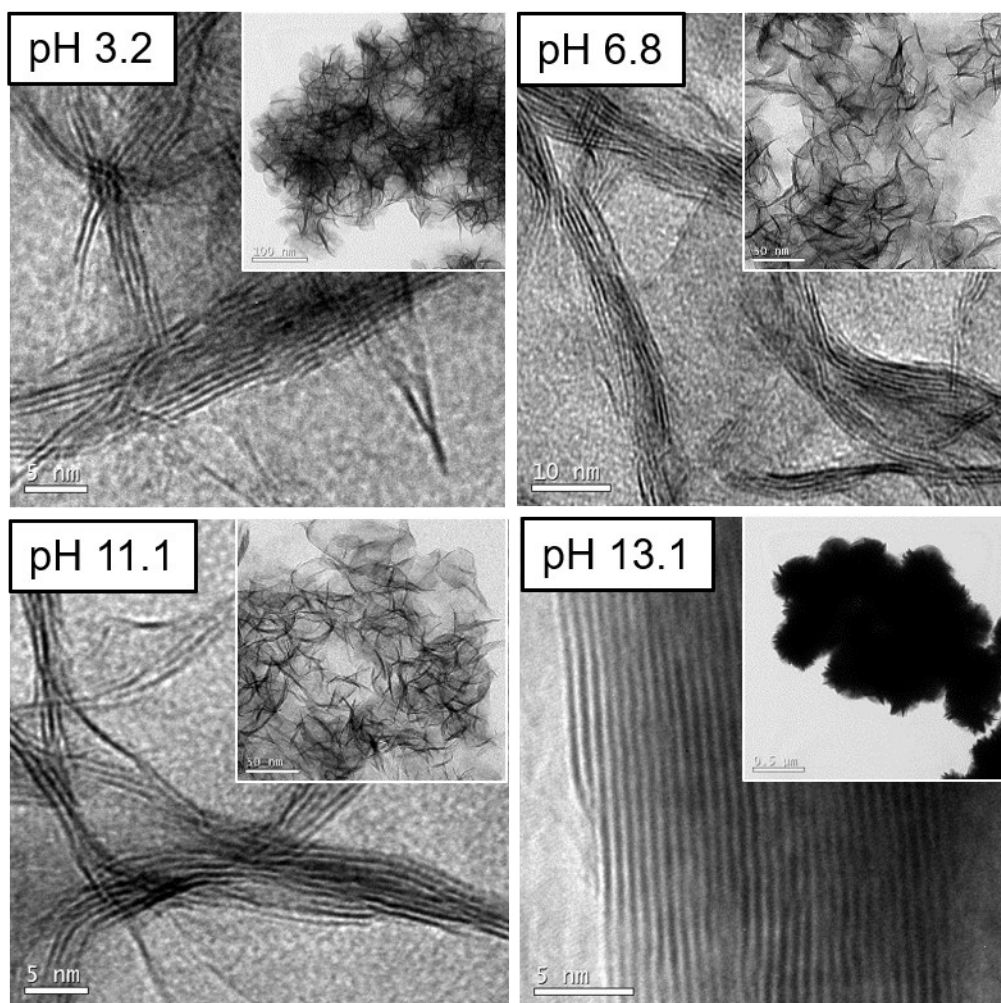


**Fig. S1** HRTEM images of MoS<sub>2</sub> layered nanostructure, synthesized under different pH (3.2, 6.8, 11.1, and 13.1).

The pH of aqueous (NH<sub>4</sub>)<sub>2</sub>MoS<sub>4</sub> solution (0.254 mmol in 20 mL, 12.7 mM) is 7. After adjusting the pH by adding aqueous KOH, H<sub>2</sub>SO<sub>4</sub>, or HCl solutions, the solvothermal reaction produced an amorphous phase at pH 0. At pH 3–11, the MoS<sub>2</sub> layered structures were synthesized. The thickness of the layers is less than 5 nm. As pH increased to 13, much thicker and larger bulk crystals were produced that were almost insoluble in water.

We explain these observed trends as follows. It is known that the thermal decomposition of  $(\text{NH}_4)_2\text{MoS}_4$  produces  $\text{MoS}_2$  in the reactions of  $(\text{NH}_4)_2\text{MoS}_4 \rightarrow \text{MoS}_4^{2-} + 2\text{NH}_4^+$  and  $\text{MoS}_4^{2-} + 2\text{NH}_4^+ \rightarrow \text{MoS}_2 + \text{S} + 2\text{NH}_3 + \text{H}_2\text{S}$ . The addition of  $\text{H}^+$  can catalyze the decomposition by the reaction of  $\text{MoS}_4^{2-} + 2\text{H}^+ \rightarrow \text{MoS}_2 + \text{H}_2\text{S} + \text{S}$ , producing efficiently the thin layered nanostructures. At the higher pH, the decomposition reaction of  $(\text{NH}_4)_2\text{MoS}_4$  becomes retarded. At pH 13, the bulk form is produced with the slower reaction rate.

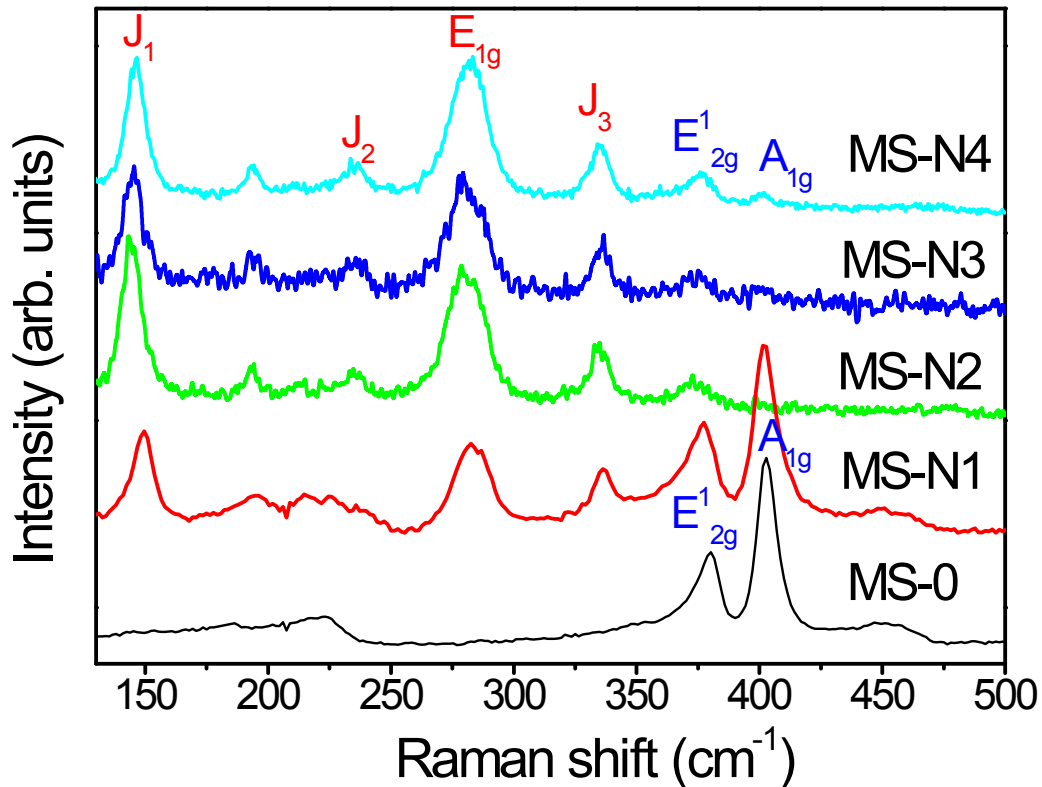


**Fig. S2** Raman spectrum of the samples. Excitation laser is 532 nm diode laser.

The MS-0 exhibit the characteristic Raman peaks of the 2H phase at 380 and 403  $\text{cm}^{-1}$  corresponding to the in-plane  $E^1_{2g}$  and out-of-plane  $A_{1g}$  vibration modes, respectively. The Raman spectra of intercalated  $\text{MoS}_2$  (MS-N1 ~ -N4) show three typical peaks of the distorted 1T' phase: the  $J_1$  peak at 148  $\text{cm}^{-1}$ , the  $J_2$  peak at 236  $\text{cm}^{-1}$ , and the  $J_3$  peak at 336  $\text{cm}^{-1}$ .<sup>S18</sup> The  $E_g$  vibration mode peak appears at 284  $\text{cm}^{-1}$ . Therefore, the intercalated samples consisted of the 1T' phase.

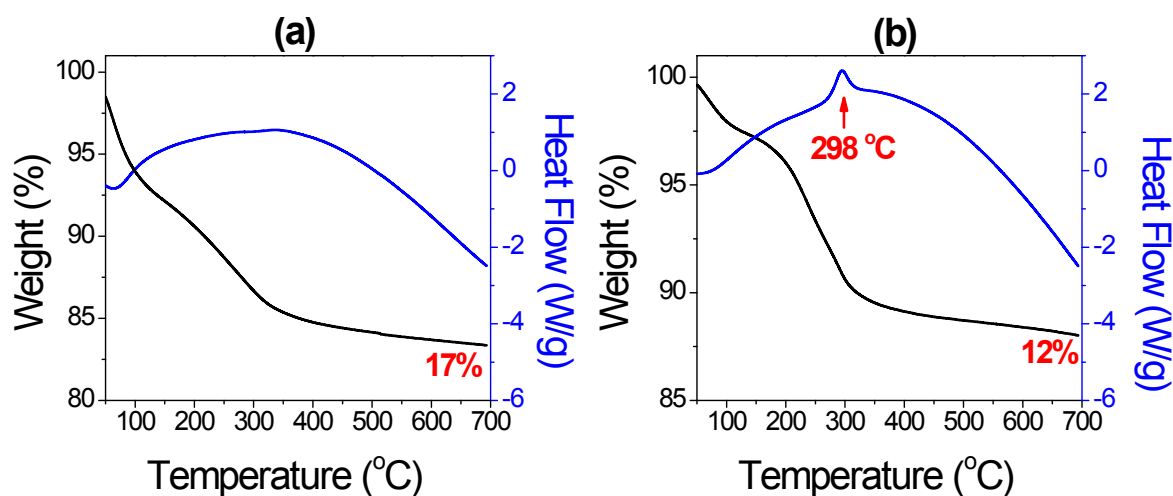


**Fig. S3** TGA and DSC data of (a) MS-0 and (b) MS-N4. The samples were heated from room temperature to 700 °C at 10 °C/min and under N<sub>2</sub> flow (100 sccm).

Thermogravimetric analysis (TGA) curve of MS-0 shows a total loss of 17% at 700 °C, which can be divided into the partial losses of 6% at 25–100 °C, 9% at 100–340 °C, and 2% between 340 and 700 °C. The differential scanning calorimetry (DSC) curve shows an endothermic peak at 66 °C, corresponding to the first weight loss step, which is ascribed to the release of adsorbed species such as water. The second weight loss of 10% is probably due to the intercalated water and ammonium ions that originated from the precursors.

MS-N4 shows 3% weight losses in the 50-150 °C range, 7% at 130-300 °C, and 2% between 300 and 700 °C, with a total weight loss of 12%. The DSC curve shows an endothermic peak at 90 °C corresponding to the release of adsorbates. An exothermic peak, not observed for MS-0, emerges at 298 °C. This peak could be due to the transformation from the 1T' to the 2H.<sup>S19</sup>

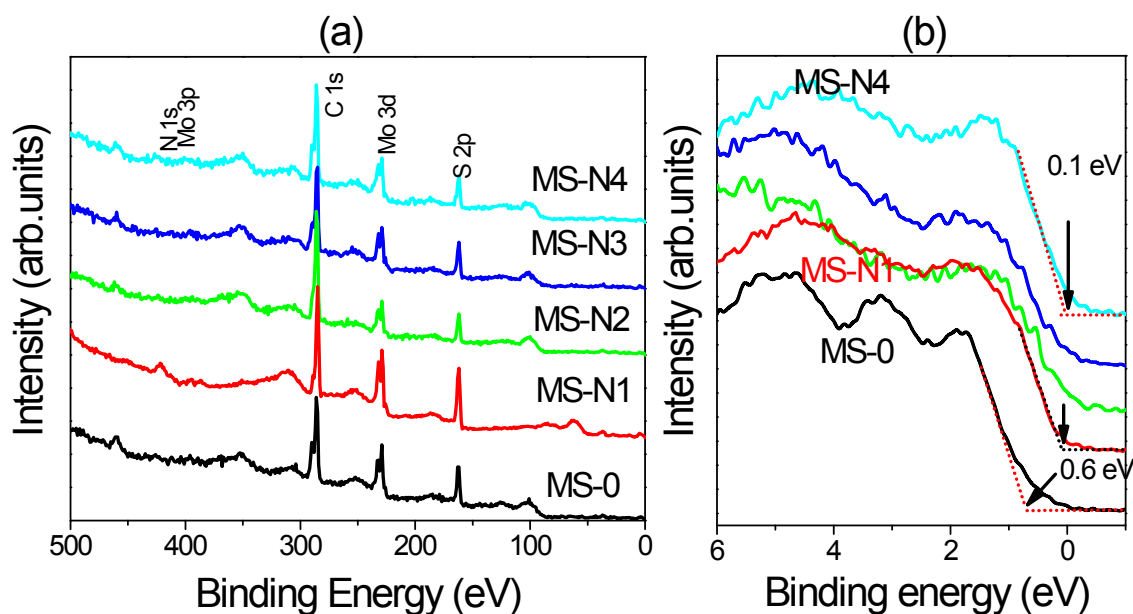


**Fig. S4** (a) XPS survey scans and (b) valence spectrum of samples (MS-0 and MS-N1~N4).

(a) The C peak of MS-N1~N4 is larger than that of MS-0, due to the amine molecules.

(b) The positions of the valence band maximum (VBM) were evaluated by linear extrapolation of the onset in the XPS valence band (VB) spectra. The zero-binding energy was calibrated using the work function of Au metal. The VBM value of the 2H phase MS-0 is 0.6 eV. As the amines were intercalated, the VBM was redshifted to 0.1 eV, respectively, which supports the production of the metallic 1T' phase.

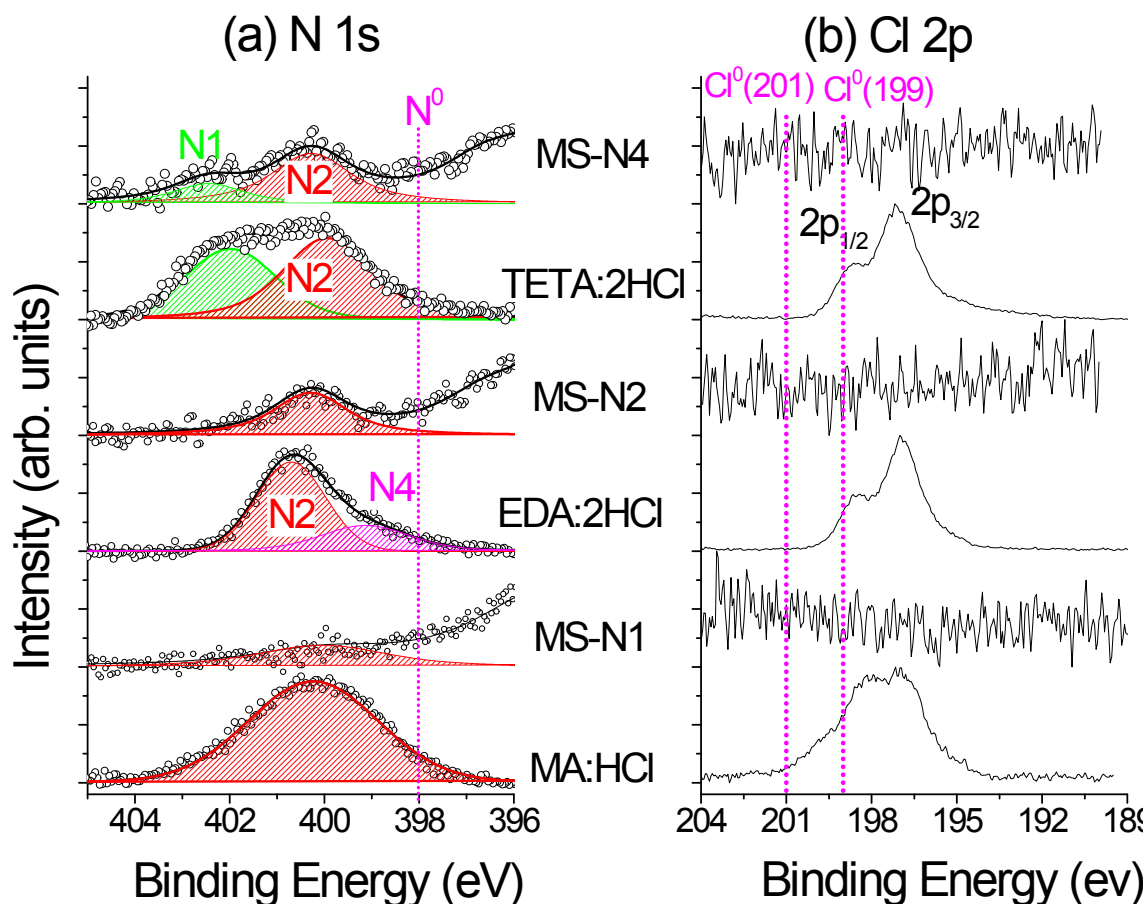


**Fig. S5** XPS spectra of MA·HCl, MS-N1, EDA·2HCl, MS-N2, TETA·2HCl, and MS-N4 for (a) N 1s and (b) Cl 2p peaks.

Figure S5a shows the N 1s peak for the intercalated MoS<sub>2</sub> samples and amine HCl salt powders. In the case of TETA·2HCl, the peak was resolved into two bands at 402 eV (N1 band) and 400 eV (N2 band), which are blue-shifted with respect to the signal of neutral N (N<sup>0</sup>) at 398.1 eV. The ratio of the two bands is close to 1, so the N1 and N2 bands are assigned to -NH<sub>2</sub> (primary N) and -NH- (secondary N) bonds, respectively. MS-N4 shows the N1 and N2 bands at the same positions as TETA·2HCl. The ratio of N1/N2 decreases to 0.5, suggesting that the NH<sub>2</sub> terminal group may release a hydrogen to become a secondary-like amino group (N2 band) or the dissociation of NH<sub>2</sub> group may supply the N atoms for the doping into the MoS<sub>2</sub>.

For EDA·2HCl, the peak was resolved into two bands at 400.6 (N2 band) and 399 eV (N4 band). The ratio of N2/N3 is larger than 5, so the N2 band is assigned to NH<sub>2</sub>. The N4 band

probably comes from the charging problem due to a lower conductivity of the powder. In the EDA-intercalated MoS<sub>2</sub>, the peak appears at 400.4 eV, which is similar to the N2 band of EDA·2HCl. In the case of MA·HCl, the peak appears at 400.2 eV. The MA-intercalated MoS<sub>2</sub> shows a band at 400.1 eV, similar to that of MA·HCl. As shown in Figure 5b, there are no Cl peaks in the intercalated MoS<sub>2</sub> samples. The 2p<sub>3/2</sub> and 2p<sub>1/2</sub> of amine salt are red shifted from the neutral ones (199 and 201 eV) by 1.9 eV.

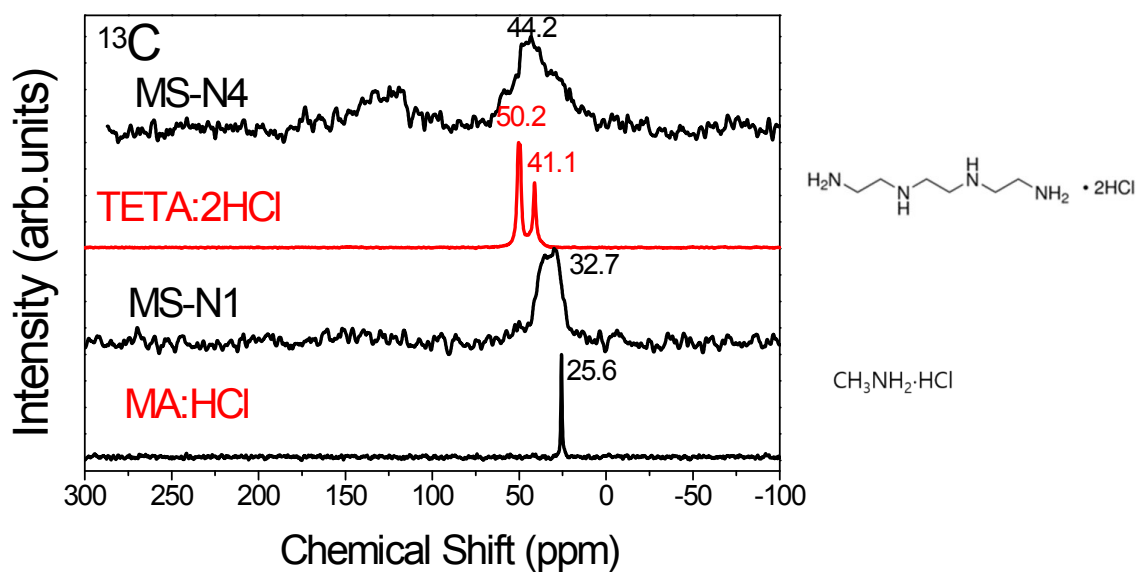


**Fig. S6** Solid state  $^{13}\text{C}$  NMR spectra of MA:HCl, MS-N1, TETA:2HCl, and MS-N4.

MA:HCl and MS-N1 show the  $\text{CH}_3$  peak at 25.6 and 32.7 ppm, respectively. TETA:2HCl shows two peaks at 50.2 and 41.1 ppm, with a ratio of 2:1 that originates from the four  $-\text{C}-\text{NH}$  and two  $-\text{C}-\text{NH}_2$ . For MS-N4, the broader peak appears at 44.2 ppm and is assigned to the TETA. The peak at 128 ppm may originate from the background due to the low signal-to-noise ratio. The peak broadening and shift are probably due to the electrostatic interaction with  $\text{MoS}_2$ . Therefore, the MA and TETA molecules exist in the interlayers of  $\text{MoS}_2$ .

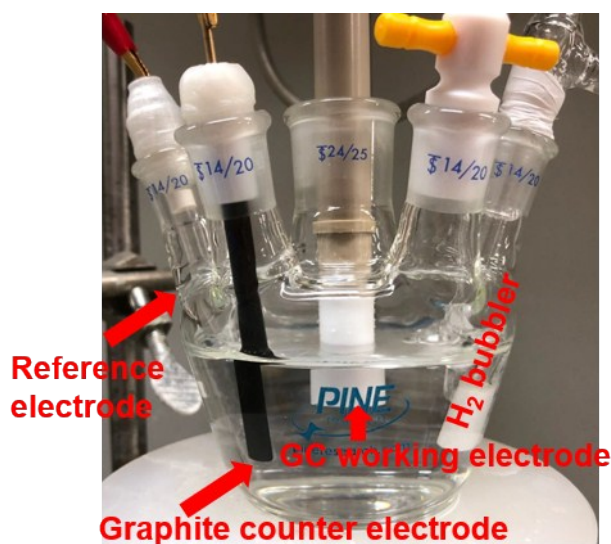
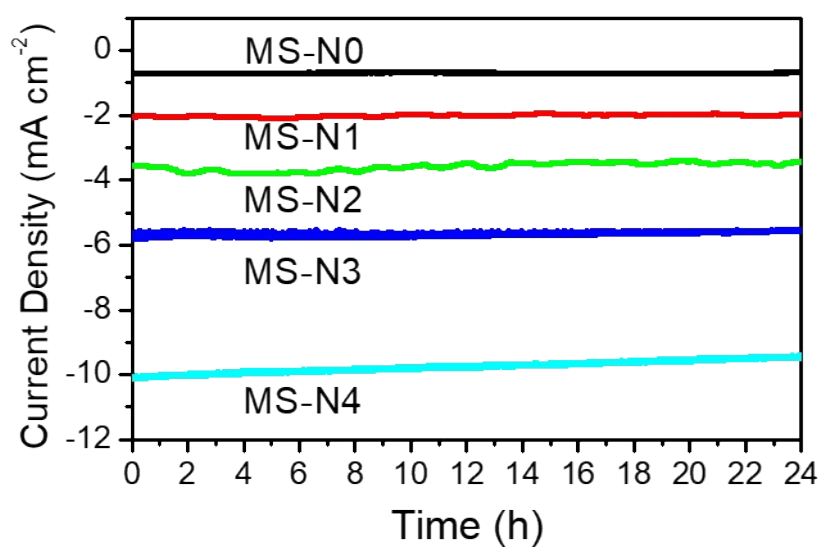


**Fig. S7** Chronoamperometric responses of MS-N0, MS-N1, MS-N2, MS-N3, and MS-N4 (at 0.16 V), showing a current attenuation of ~3% after 24 h. Photograph shows the cell setup when the graphite rod was used as counter electrode. The counter electrode was shielded by a membrane that blocks the transmission of dissolved C ions or carbon particles into the electrolyte.

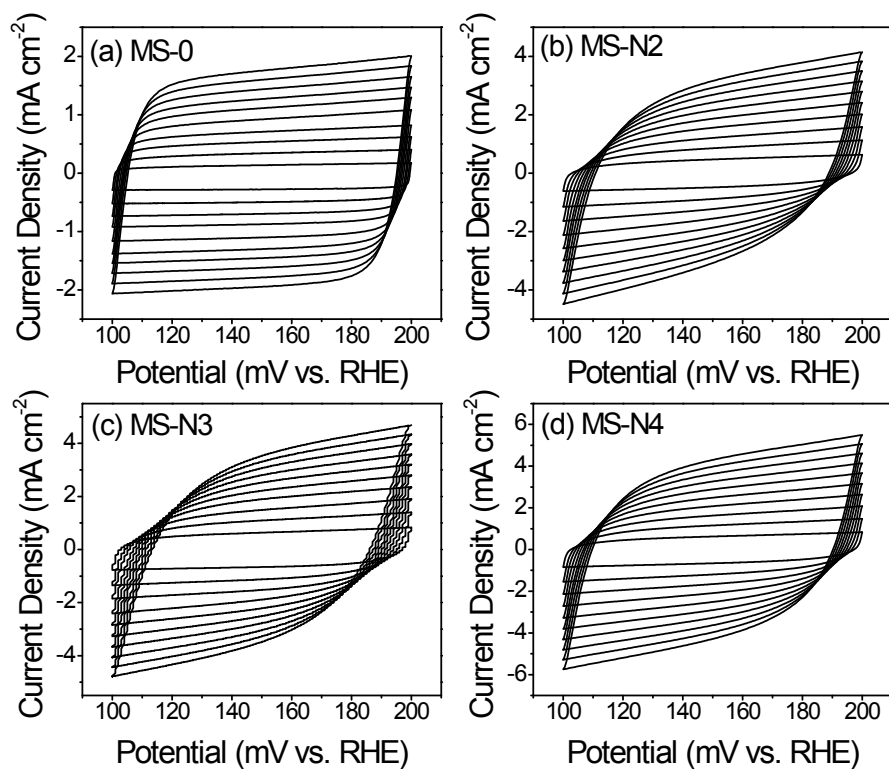


**Fig. S8** Cyclic voltammograms of (a) MS-0, (b) MS-N2, (c) MS-N3, and (d) MS-N4 in a non-Faradaic region (0.1-0.2 V vs. RHE), at 20-200  $\text{mV s}^{-1}$  scan rates (with a step of 20  $\text{mV s}^{-1}$ ) and in 0.5 M  $\text{H}_2\text{SO}_4$  solution.

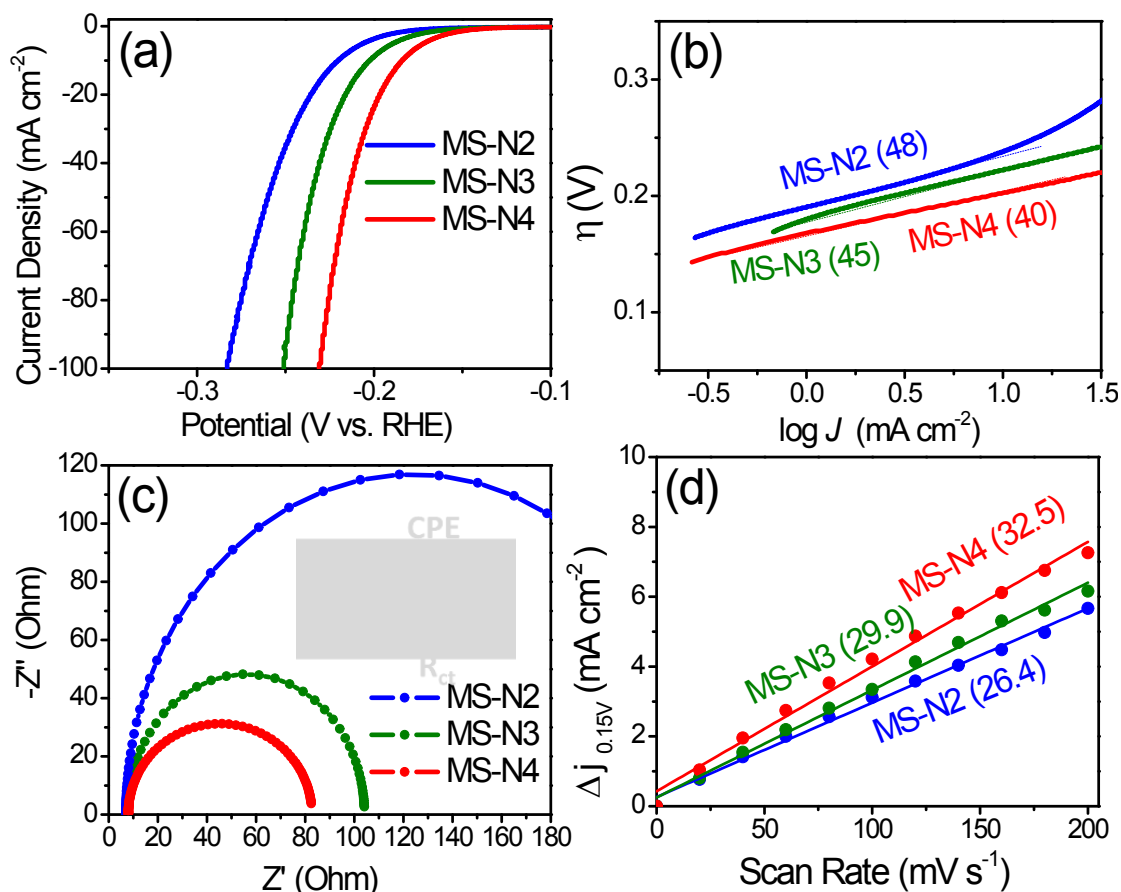


**Fig. S9** (a) LSV curves (scan rate:  $2 \text{ mV s}^{-1}$ ) for MS-N2, MS-N3, and MS-N4 (synthesized at pH 11.1, 11.2, and 11.3, respectively) as catalysts toward HER in  $\text{H}_2$ -saturated  $0.5 \text{ M H}_2\text{SO}_4$ . (b) Tafel plots derived from the LSV curves. The number in the parenthesis represents the Tafel slope in  $\text{mV dec}^{-1}$ . (c) Nyquist plots for EIS measurements from  $100 \text{ kHz}$  to  $0.1 \text{ Hz}$  at a representative potential of  $-0.15 \text{ V}$  (vs. RHE) and the equivalent circuit diagram (inset). (d) Difference between the anodic charging and cathodic discharging currents of CV ( $\Delta j$ ) measured at  $0.15 \text{ V}$  (vs. RHE) and plotted as a function of the scan rate.

The applied potentials that delivered a current density of  $10 \text{ mA cm}^{-2}$  ( $\eta_{j=10}$ ) were  $0.26$ ,  $0.22$ ,  $0.20$ , and  $0.18 \text{ V}$  for MS-N2, MS-N3, and MS-N4, respectively. Tafel plots obtained from the low potential region ( $\eta = -0.25 - 0.15 \text{ V}$ ) show that the Tafel slopes of  $48$ ,  $45$ , and  $40 \text{ mV dec}^{-1}$  for MS-N2, MS-N3, and MS-N4, respectively. EIS data in the frequency range of  $100 \text{ kHz} - 0.1 \text{ Hz}$  with an amplitude of  $10 \text{ mV}$  at  $\eta = 0.15 \text{ V}$  were fitted by a Randles circuit (inset), yielding  $R_{ct} = 230$ ,  $104$ , and  $83 \Omega$  for MS-N2, MS-N3, and MS-N4, respectively. The CV curves were measured at  $0.1 - 0.2 \text{ V}$ , in a non-Faradaic region using various scan rates ( $20 - 200 \text{ mV s}^{-1}$ ). The  $\Delta j$  was obtained as the difference between the anodic charging (positive value) and cathodic

discharging currents (positive value), and plotted as a function of scan rate. The slope of a linear fit provides twice of the double-layer capacitance ( $2C_{dl}$ ) of 26.4, 29.9, and 32.5 mF cm<sup>-2</sup>, respectively for MS-N2, MS-N3, and MS-N4. Therefore, the respective  $C_{dl} = 13.2, 15.0,$  and 16.3 mF cm<sup>-2</sup>. The data are summarized in Table S4.

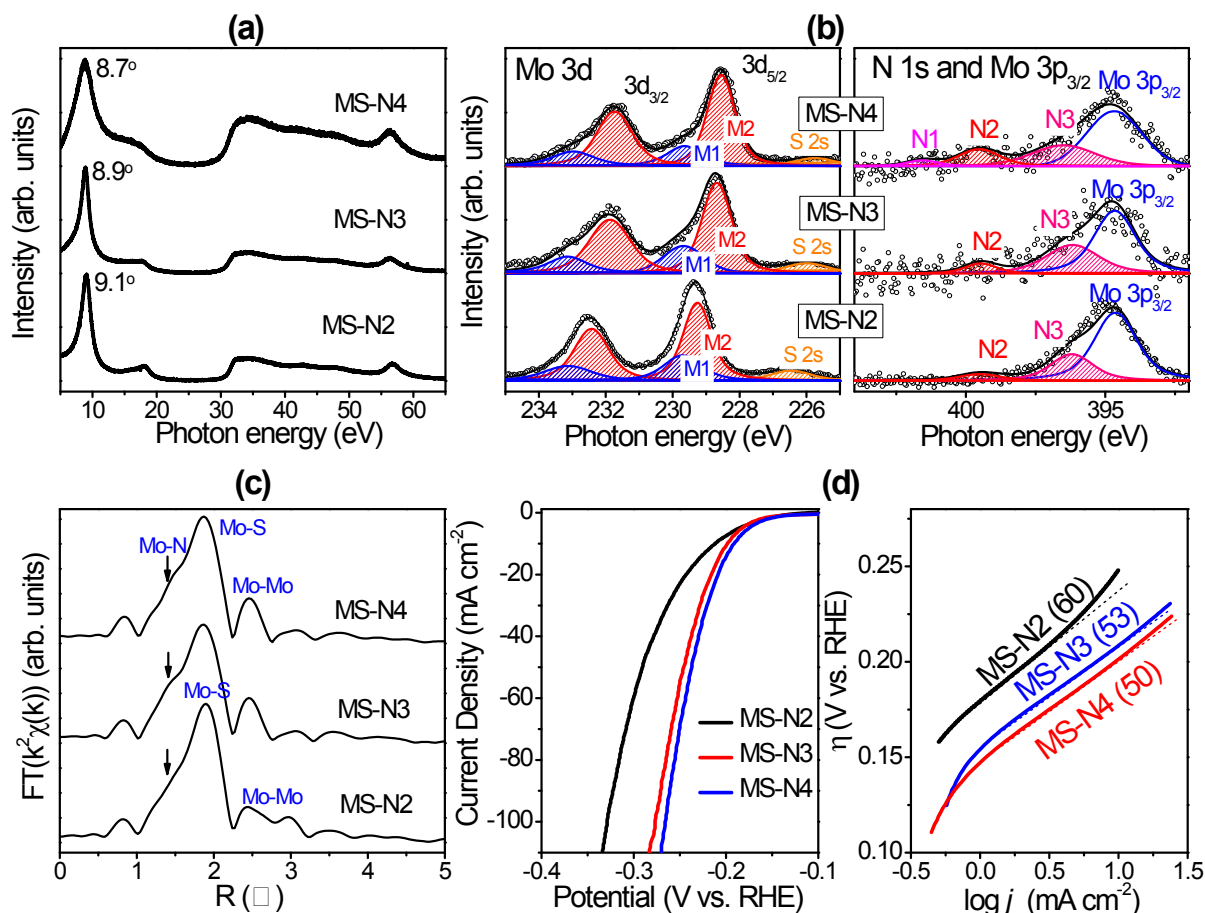


**Fig. S10.** (a) XRD patterns of MS-N2, MS-N3, and MS-N4 synthesized at 220 °C. (b) Fine-scan XPS Mo 3d, N 1s and Mo 3p<sub>1/2</sub> peaks. The XPS data (open circles) are fitted by a Voigt function, and the sum of the resolved bands is represented by a black line. (c) Fourier-transformed EXAFS spectra at the Mo K edge. (d) LSV curves (scan rate: 2 mV s<sup>-1</sup>) for MS samples in H<sub>2</sub>-saturated 0.5 M H<sub>2</sub>SO<sub>4</sub>, and Tafel plots derived from the LSV curves. The number in the parenthesis represents the Tafel slope in mV dec<sup>-1</sup>.

(a) The position of the (002) peak shifts significantly to the lower angle. The (002) peak of MS-N2, MS-N3, and MA-N4 is shifted to lower  $2\theta$  angles of 9.1°, 8.9°, and 8.7°, respectively. The intercalation leads to an increase of the  $c$  value to 19.3, 20.2, and 20.6 Å upon increasing the N numbers, in agreement with the samples synthesized at 200 °C.

(b) The Mo 3d<sub>3/2</sub> and 3d<sub>5/2</sub> peaks (separated by about 3 eV) were resolved using a Voigt function. MS-N2 shows a 3d<sub>5/2</sub> peak at 229.4 eV, which can be assigned to the Mo ions in the 2H phase of MoS<sub>2</sub>. In contrast, the 3d<sub>5/2</sub> peak is located at 228.7 and 228.6 eV in MS-N3 and MS-N4, respectively, corresponding to the 1T' phase. In MS-N3 and MS-N4, the concentration

of intercalated amine ( $C_A$ ) is 3% and 6%, respectively. The concentration of S vacancies ( $C_{VS}$ ) is 24%, 24%, and 25% for MS-N2, MS-N3, and MS-N4, respectively.

The N 1s peak was resolved into three bands: N1 band at 402.5 eV, N2 band at 400 eV, and N3 band 396.5 eV, corresponding to the  $-NH_2$  and  $-NH-$  of the intercalated amine molecules and the Mo-N bonding structures, respectively. MS-N2 shows negligible amount of intercalated EDA molecules. In MS-N2, MS-N3, and MS-N4, the concentration of intercalated amine ( $C_A$ ) is 1%, 3%, and 6%, respectively, and the concentration of doped N atoms ( $C_{ND}$ ) is 20%, 22%, and 30%.

(c) Fourier-transform (FT) EXAFS peaks indicate the distances to nearest neighbor atoms. The distance of Mo-N, Mo-S, and Mo-Mo bonds is 2.0, 2.40 and 2.76 Å, respectively, corresponding to those of N-doped 1T' phase.

(d) The applied potentials that delivered a current density of 10 mA cm<sup>-2</sup> ( $\eta_{j=10}$ ) were 0.21, 0.19, and 0.19 V for MS-N2, MS-N3, and MS-N4, respectively, and the Tafel slopes are 60, 53, and 50 mV dec<sup>-1</sup>.

The present results showed that all three samples are doped with ~25% N atoms, which is about the same as those of MS-N2, MS-N3, and MS-N4 synthesized at 200 °C. As the concentration of intercalated amine molecules is reduced significantly to 1%, 3%, and 6% for N2, N3, and N4, the HER performance decreased compared to that with 10% amine intercalation (MS-N2, MS-N3, and MS-N4 synthesized at 200 °C). Therefore, we conclude that the amine intercalation plays an important role in the catalytic activity toward the HER.

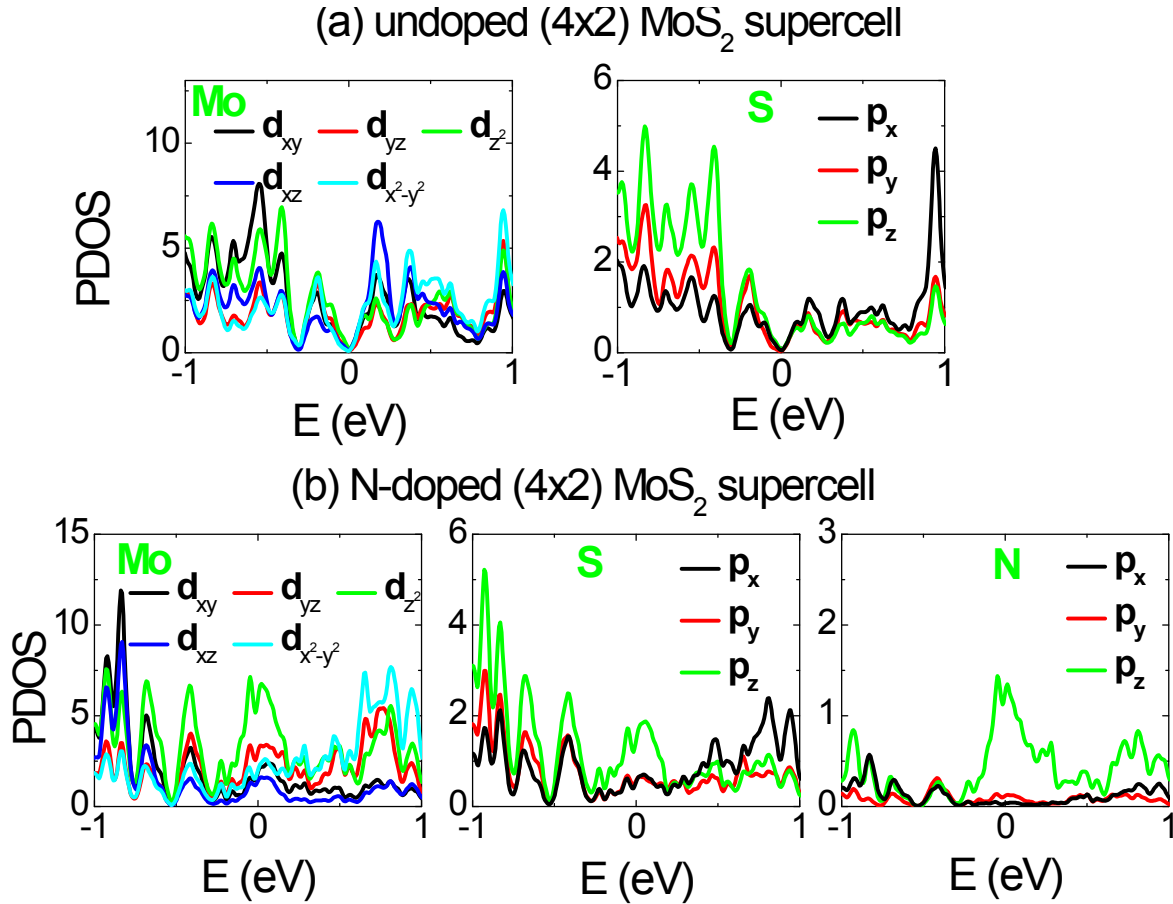


**Figure S11.** PDOS of Mo, S, and N atoms for (a) undoped and (b) 25% N-doped (4×2) MoS<sub>2</sub> supercells (with  $C_{VS} = 25\%$ ).

When the N atoms are doped without intercalation, the partial DOS (PDOS) of  $p_z(N)$  states are only partially occupied, indicating that the electrons are not isolated as lone pair but have strong interaction with the orbitals of adjacent atoms. The  $d_{z^2}(\text{Mo})$  states, which take part in the Mo-N bonding, become destabilized by an electrostatic repulsion by the  $d_{xy}(\text{Mo})$  electrons, being shifted upward in such a way that the PDOS of  $d_{z^2}(\text{Mo})$  states is also appreciably enhanced around the Fermi level. In this regard, we note that two of three Mo-N bonds from a given Mo ion are defined to be diagonal to the X and Y axes in our coordinate system, so that the Mo-N bond formations are mediated by the  $d_{xy}(\text{Mo})$  orbitals. Likewise, the  $p_z(\text{S})$  states are also enhanced. Therefore, the enhanced TDOS of N-doped MoS<sub>2</sub> (as shown in Figure 7b in the manuscript) is due to the strong overlap of  $d_{z^2}(\text{Mo})$ ,  $p_z(\text{S})$ , and  $p_z(\text{N})$  states. This observation leads us to conjecture that electron transport on the MoS<sub>2</sub> layers can be enhanced appreciably, which will be much less pronounced in the absence of the N doping.

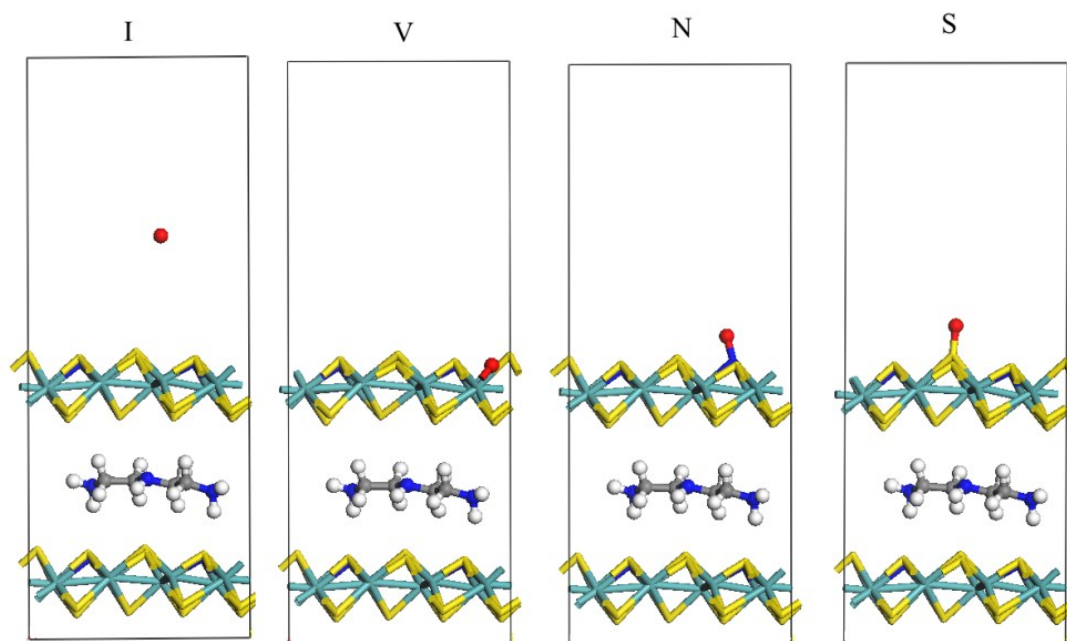


**Fig. S12.** Structures of (4×2) MS-N3T system in configuration A: initial (I) and final three adsorption sites (V, N, and S) of a H<sup>+</sup> ion for Volmer reaction.

Recalling that the dominant mechanism of the HER was Volmer reaction followed by Heyrovsky reaction, we calculated the reaction path for the Volmer reaction on the surface of (4×2) MS-N3T system in configuration A. For simplicity, we employed a slab geometry in which a supercell includes two (4×2) MoS<sub>2</sub> layers and one intercalated DETA molecule. The adsorption energies and activation barriers for three different adsorption sites of a H<sup>+</sup> ion were calculated using the climbing image-nudged elastic band (CINEB) method.<sup>S20</sup> The adsorption on the V, S, and N sites represent that the H<sup>+</sup> ion is attached on top of a S vacancy, a S atom, and a N atom, respectively. The Mo ions on the bottom layer were fixed, while all other atoms were allowed to relax freely.

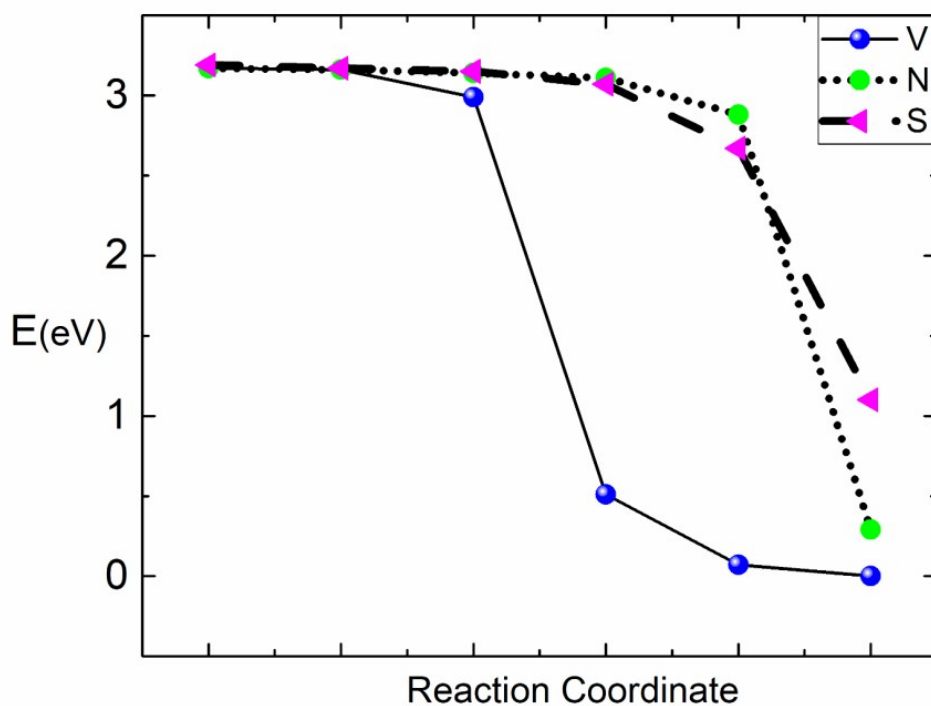


**Fig. S13.** Relative energy of (4×2) MS-N3T system in configuration A versus reaction coordinate of three adsorption sites for Volmer reaction.

The reaction paths for V, S, and N sites indicate that none of them experiences a barrier. Therefore, the preferable adsorption site can be primarily understood in terms of the relative stabilities of the three sites in Volmer reaction. It is interesting to note that the V site is the most stable, and the N site is 0.30 eV less stable. On the other hand, the S site is the least stable, i.e., by 1.10 eV with respect to the V site. This result is consistent with our experimental observation that the HER is more enhanced at the higher S vacancies.

#### IV. References

- S1.** J. Xie, H. Zhang, S. Li, R. Wang, X. Sun, M. Zhou, J. Zhou, X. W. Lou and Y. Xie, *Adv. Mater.*, 2013, **25**, 5807-5813.
- S2.** D. Voiry, M. Salehi, R. Silva, T. Fujita, M. Chen, T. Asefa, V. B. Shenoy, G. Eda and M. Chhowalla, *Nano Lett.*, 2013, **13**, 6222-6227.
- S3.** J. Xie, J. Zhang, S. Li, F. Grote, X. Zhang, H. Zhang, R. Wang, Y. Lei, B. Pan and Y. Xie, *J. Am. Chem. Soc.*, 2013, **135**, 17881-17888.
- S4.** M. Gao, M. K.Y. Chan and Y. Sun, *Nat. Commun.*, 2015, **6**, 7493.
- S5.** H. Li, C. Tsai, A. L. Koh, L. Cai, A. W. Contryman, A. H. Fragapane, J. Zhao, H. S. Han, H. C. Manoharan, F. A. Pedersen, J. K. Nørskov and X. Zheng, *Nat. Mater.*, 2015, **15**, 48-53.
- S6.** Z. Wu, C. Tang, P. Zhou, Z. Liu, Y. Xu, D. Wang and B. Fang, *J. Mater. Chem. A*, 2015, **3**, 13050-13056.
- S7.** D. Voiry, R. Fullon, J. Yang, C. C. C. Silva, R. Kappera, I. Bozkurt, D. Kaplan, M. J. Lagos, P. E. Batson, G. Gupta, A. D. Mohite, L. Dong, D. Er, V. B. Shenoy, T. Asefa and M. Chhowalla, *Nat. Mater.*, 2016, **15**, 1003–1009.
- S8.** X. Geng, W. Sun, W. Wu, B. Chen, A. A. Hilo, M. Benamara, H. Zhu, F. Watanabe, J. Cui and T. Chen, *Nat. Commun.*, 2016, **7**, 10672.
- S9.** Y. Yin, J. Han, Y. Zhang, X. Zhang, P. Xu, Q. Yuan, L. Samad, X. Wang, Y. Wang, Z. Zhang, P. Zhang, X. Cao, B. Song and S. Jin, *J. Am. Chem. Soc.*, 2016, **138**, 7965-7972.
- S10.** F. Z. Wang, M. J. Zheng, B. Zhang, C. Q. Zhu, Q. Li, L. Ma and W. Z. Shen, *Sci. Rep.*, 2016, **6**, 31092.
- S11.** Y. Kim, D. H. K. Jackson, D. Lee, M. Choi, T. W. Kim, S. Y. Jeong, H. J. Chae, H. W. Kim, N. Park, H. Chang, T. F. Kuech and H. J. Kim, *Adv. Funct. Mater.*, 2017, **27**, 1701825.
- S12.** J. Zhang, J. Wu, H. Guo, W. Chen, J. Yuan, U. Martinez, G. Gupta, A. Mohite, P. M. Ajayan and J. Lou, *Adv. Mater.*, 2017, **29**, 1701955.
- S13.** D. Wang, X. Zhang, S. Bao, Z. Zhang, H. Feia and Z. Wu, *J. Mater. Chem. A*, 2017, **5**, 2681–2688.
- S14.** Y. Shi, Y. Zhou, D. R. Yang, W. X. Xu, C. Wang, F. B. Wang, J. J. Xu, X. H. Xia and H. Y. Chen, *J. Am. Chem. Soc.*, 2017, **139**, 15479-15485.

**S15.** E. E. Benson, H. Zhang, S. A. Schuman, S. U. Nanayakkara, N. D. Bronstein, S. Ferrere, J. L. Blackburn and E. M. Miller, *J. Am. Chem. Soc.*, 2018, **140**, 441–450.

**S16.** C. Tan, Z. Luo, A. Chaturvedi, Y. Cai, Y. Du, Y. Gong, Y. Huang, Z. Lai, X. Zhang, L. Zheng, X. Qi, M. H. Goh, J. Wang, S. Han, X. Wu, L. Gu, C. Kloc and H. Zhang, *Adv. Mater.*, 2018, **30**, 1705509.

**S17.** J. Luxa, P. Vosecky, V. Mazanek, D. Sedmidubsky, M. Pumera, Z. Sofer, *ACS Catalysis* 2018, **8**, 2774-2781.

**S18.** D. Yang, S. J. Sandoval, W. M. R. Divigalpitiya, J. C. Irwin and R. F. Frindt, *Phys. Rev. B*, 1991, **43**, 12053-12056.

**S19.** J. Xie, J. Zhang, S. Li, F. Grote, X. Zhang, H. Zhang, R. Wang, Y. Lei, B. Pan and Y. Xie, *J. Am. Chem. Soc.* 2013, **135**, 17881-17888.

**S20.** G. Henkelman and H. Jónsson, *J. Chem. Phys.* 2000, **113**, 9901-9904.